

Winter to summer monsoon variation of aerosol optical depth over the tropical Indian Ocean

F. Li and V. Ramanathan

Center for Clouds, Chemistry and Climate, Scripps Institution of Oceanography, University of California, San Diego, La Jolla, California, USA

Received 14 June 2001; revised 4 December 2001; accepted 19 December 2001; published 22 August 2002.

[1] The northern Indian Ocean undergoes a major transition from anthropogenic aerosols during the northeasterly winter monsoon season to mineral dust and sea salt during the southwest summer monsoon. The former is dominated by low-level transport from south and southeast Asia, while the latter results from low to mid tropospheric transport from the African continent and the Arabian Peninsula. During the winter monsoon, low-level transport from the Indian subcontinent and neighboring nations is particularly important. This paper uses 5 years of satellite-derived aerosol optical depths (AODs) to document the large seasonal variations in AODs modulated by the monsoons. In situ data are used to develop and validate the procedure we employ to derive visible AODs from the radiances observed by the advanced very high resolution radiometer (AVHRR) onboard polar-orbiting satellites. Monthly mean AOD over the Arabian Sea displays a clear annual cycle with a maximum (0.60 ± 0.10) in July and a minimum (0.20 ± 0.05) in January. The summer monsoon maximum is due both to the southwest winds bringing dust from the Horn of Africa over the Arabian Sea and mid tropospheric transport of dust from the Arabian Peninsula. Such long-range transports also lead to aerosol loading south of the equator. We also show that the Indonesia forest fires during the 1997 El Niño led to a large increase in AOD over most of the equatorial Indian Ocean. *INDEX TERMS:* 0305

Atmospheric Composition and Structure: Aerosols and particles (0345, 4801); 0360 Atmospheric Composition and Structure: Transmission and scattering of radiation; 1640 Global Change: Remote sensing; *KEYWORDS:* aerosols and particles, transmission and scattering of radiation, remote sensing

1. Introduction

[2] The tropical Indian Ocean is influenced by two contrasting air masses (continental and marine) associated with the Indian monsoon system. The summer monsoon, also known as the southwest monsoon, usually starts by the end of May and continues until November. During this period, winds are mainly southwesterly or westerly. The winter monsoon (also called the northeast monsoon) becomes established toward the end of November and continues until April. During this period the prevailing winds are mostly northeasterly. This study examines how the two contrasting monsoonal air masses influence the regional aerosol distribution. During the winter monsoon period, anthropogenic trace species and their reaction products (e.g., sulfates and ozone) from the Northern Hemisphere are directly connected to the pristine air of the Southern Hemisphere by a cross-equatorial monsoonal flow into the Intertropical Convergence Zone (ITCZ) [Ramanathan *et al.*, 2001]. The analysis during the winter monsoon revealed that the AOD distributions over the ocean are dominated by anthropogenic aerosols [Rajeev *et al.*, 2000; Ramanathan *et al.*, 2001]. This paper completes the picture

by describing the aerosol optical depth (AOD) during the full annual cycle.

[3] Using the observed single scattering albedo (SSA), and phase function derived from in situ data, Rajeev *et al.* [2000] studied the spatial distribution of aerosol optical depth over the tropical Indian Ocean based on AOD retrieved from advanced very high resolution radiometer (AVHRR) visible channel radiances during January to March 1998. The aerosol scattering phase function and SSA used in the retrieval were obtained by integrating surface aerosol optical depths and a comprehensive aerosol model [Satheesh *et al.*, 1999]. The data were collected during February to March 1998 as part of the first field phase (FFP) of the Indian Ocean Experiment (INDOEX) [Ramanathan *et al.*, 1995, 1996]. INDOEX focuses on studying the long-range transport of trace species and aerosols from urban regions and assessing their direct and indirect radiative forcing.

[4] In this study we have made several improvements to the Rajeev *et al.* [2000] algorithm along the following lines: incorporated new sensor calibration coefficients obtained from Tahnk [2001]; added a correction term for water-leaving radiance; introduced a correction for contamination of clear radiances by thin cirrus; and adopted a seasonal variation in the aerosol SSA and a composition-related phase function. With the improved retrieval method, 5-year AOD over the INDOEX area (30°N to

$\sim 35^{\circ}\text{S}$, 40°E to $\sim 100^{\circ}\text{E}$) have been derived from the NOAA 14/AVHRR global area coverage (GAC) data during 1 January 1996 to 31 December 2000. In section 2 the retrieval procedure and its improvements are presented. With more than 2 years data for validation, comparison of the retrieved AOD to ground-based AOD measurements is given in section 3. The patterns of seasonal and interannual variation of AODs over the tropical Indian Ocean are described in section 4.

2. Data Analyses

2.1. Data and Method of Analysis

[5] We have used the NOAA 14/AVHRR GAC data for the afternoon satellite pass in 2600-km-wide swaths over the Indian Ocean. The spatial resolution of GAC data is 1.1×4 km at nadir, sampled every third scan line, although generally treated as 4-km resolution. AVHRR has five wavelength bands of observation, namely, visible (channel 1, $\approx 580\text{--}680$ nm); near infrared (channel 2, $\approx 720\text{--}1100$ nm); and infrared (channel 3, $\approx 3.5\text{--}4.0$ μm) and channel 4, $\approx 10.5\text{--}11.5$ μm and channel 5, $\approx 11.5\text{--}12.5$ μm). Channel 1 radiances are used for retrieving AOD over the ocean areas. Brightness temperatures derived from channels 4 and 5, along with radiance from channels 1 and 2, are used for cloud detection. Fresnel reflection of the direct and diffuse solar radiation at the ocean surface varies with wind speed and is calculated for rough ocean on the basis of the model proposed by *Cox and Munk* [1954]. This model gives probability distribution of surface slopes as a function of wind speed and direction. Magnitude of the surface reflectance and its variation with wind speed are maximum at the solar side of satellite scan, and the error in retrieved AOD will be larger in this region because of the uncertainty in the actual wind speed. To minimize the effect of specular reflection from the ocean surface, only the antisolar side of the scan line has been included in the analysis. Reflectance of radiation at ocean surface at each pixel is based on daily surface wind speeds obtained from the National Centers for Environmental Prediction (NCEP)/National Center for Atmospheric Research (NCAR) reanalysis (2.5° horizontal resolution).

[6] The retrieval algorithm employs the aerosol model developed by *Satheesh et al.* [1999]. The Satheesh et al. model is based on the chemical, microphysical, and optical properties of aerosols derived from the INDOEX data archives. However, these observations are valid only for the winter monsoon period. The observed mean SSA at 0.55 μm for the first 1 km from the surface is ~ 0.90 and corresponds to a mean relative humidity of 78% observed during the period. The mean relative humidity varies with height, which results in a height variation of the SSA. The values of SSA as a function of relative humidity (RH) obtained based on the model of *Hess et al.* [1998] are 0.90 for 78%; 0.874 for RH = 70%; 0.861 for RH = 60%; 0.85 for RH = 50%; and 0.752 for RH = 35%. We have taken the average altitude profile of RH based on the balloon sonde data during the observation period as given by *Satheesh et al.* [1999] and used the corresponding altitude variation of aerosol SSA. This model has been developed for the winter season using INDOEX data. The revision of the model for the summer season is described in section 2.2.4.

2.2. Retrieval of Aerosol Optical Depth

[7] We have made the following improvements to the *Rajeev et al.* [2000] algorithm.

2.2.1. Adding New Calibration Coefficients

[8] The in-orbit performance of the AVHRR visible and near-infrared channel degrades with time, initially during storage and then because of outgassing (e.g., water vapor loss from filter interstices) and subsequently because of the continued exposure to the harsh space environment [*Che and Price*, 1992; *Kaufman and Holben*, 1993; *Rao and Chen*, 1995]. This degradation makes the use of preflight calibration coefficients unsuitable. Onboard calibrations for channels 3, 4, and 5 are performed by scheduling the sensor to view cold space and one or more internal warm blackbodies as part of its normal scan sequences in orbit, but there is no onboard calibration for channels 1 and 2. The lack of onboard calibration for channels 1 and 2 makes the visible and near-infrared band applications of the AVHRR data particularly difficult. Efforts have been made on in-flight calibration using Earth-based targets. One of the postlaunch calibrations chose the southeastern Libyan deserts as calibration sources [*Rao and Chen*, 1999]. The basic assumption is that the top-of-the-atmospheric albedo over the sites remains the same over a long period of time. In this study we adopted the approach developed by *Loeb* [1997] and *Tahnk* [2001], who used permanent ice sheets of Greenland and the Antarctic as calibration targets. The interior zones of permanent ice sheets are spatially and temporally stable. At high latitudes, there are numerous overpasses that provide acceptable viewing geometries for the determination of the calibration coefficients. A disadvantage, of course, is that high-latitude snow and ice scenes can be viewed only during the summer season. From the 5-year of data (1996–2000) for Antarctica and Greenland, *Tahnk* [2001] has developed new calibration coefficients. We have applied the new calibration coefficients to all of 1996 ~ 2000 AVHRR AOD retrievals.

2.2.2. Water-Leaving Radiance Correction

[9] Upwelling radiance from the sea surface consists of two components: a Fresnel reflection component and upwelling radiation from layers below the surface, the so-called water-leaving radiance resulting from scattering by particles in the ocean. The contribution due to water-leaving radiance at the wavelength of our interest was neglected in the *Rajeev et al.* [2000] retrieval procedure. As shown by retrievals with the Sea-viewing Wide Field-of-view Sensor [*Gordon and Wang*, 1994] and with the Medium-Resolution Imaging Spectrometer [*Moore et al.*, 1999], the water leaving radiance has a nonnegligible impact on the retrieval of visible aerosol optical depths over the oceans. For the low phytoplankton pigment concentrations the water leaving radiance can be assumed to be constant. The reflectance of phytoplankton cultures near 505 nm is nearly independent of the pigment concentration [*Duntley et al.*, 1974]. Since most of the open ocean may be considered as case 1 waters (the phytoplankton concentration $C < 0.25$ gm m^{-3}), the water-leaving radiance can be evaluated as a constant term using the experimental measurements [*Gordon and Clark*, 1981], which yield for clear water radiances (or A. Y. Morel's (The scattering of light by seawater: Experimental results and theoretical approach, translated from French by G. Halikas, 161 pp., Scripps Institution of Oceanography,

La Jolla, Calif., 1975) case I waters): 0.495, 0.280, and 0.0123 $\text{mW cm}^{-2} \mu\text{m}^{-1} \text{sr}^{-1}$, for wavelengths 520, 550, and 670 nm, respectively. We subtract this radiance (interpolated to 0.63 μm) from the total reflectance measured by the satellite sensor and perform the AOD retrieval on the corrected radiance. As shown later, this correction decreased the offset of the retrieved AOD from the measured AOD (from ground Sun photometers) by $\sim 7\%$.

2.2.3. Addition of a Thin Cirrus Test

[10] The contamination of thin cirrus in the so-called clear-sky radiance is a chronic problem in aerosol retrievals that rely on visible radiances. In our previous retrieval procedure [Rajeev *et al.*, 2000], three tests were used to detect and reject pixels partially filled and fully filled by clouds: (1) the threshold method (brightness temperatures in channels 4 and 5), (2) the spatial coherence test (brightness temperatures in channels 1 and 4), and (3) the visible and near-IR channel ratio method. In this study we added one more test for filtering out thin cirrus clouds. The temperature difference between channels 4 and 5 can be used to detect most types of clouds including semitransparent cirrus clouds because of the different emissivities of cloud at the two wavelengths [Kriebel, 1996]. For the most cloud-free pixels the maximum temperature difference between channels 4 and 5 which would be expected to be due to the temperature dependence of the Planck function is only $\sim 1^\circ\text{K}$. Saunders and Kriebel [1988] used a set of precomputed clear-sky AVHRR brightness temperatures to show the expected dependence of the temperature difference on the satellite zenith angle and the channel 4 brightness temperature. We used their Table 1 of differences to pick our clear-sky values. In other words, all pixels with a brightness temperature difference greater than the value given in their Table 1 are then identified as cloud-contaminated and removed.

2.2.4. Season-Dependent Phase Function and Single-Scattering Albedo

[11] As mentioned in section 2.1, the aerosol chemical composition ranges from mostly anthropogenic aerosols during winter and spring to mostly natural aerosol composition of dust, sea salt, and sulfates (derived from dimethyl sulfide). We account for this seasonal variation by modifying the aerosol scattering phase function and SSA model developed from the data collected during FFP/INDOEX, January to March 1998 [Satheesh *et al.*, 1999]. The Satheesh *et al.* aerosol model was constructed from the spectral column aerosol optical depth measurements using the CIMEL radiometer [Holben *et al.*, 1998] and size-resolved aerosol chemical measurements at the surface. This aerosol model contains seven aerosol types, namely, sea salt, sulfate, nitrate, organics, ammonia, dust, and soot. Each of these components is assumed to have lognormal size distribution, and the observed mean SSA at surface is ~ 0.88 [Ramanathan *et al.*, 2001]. During summer, however, in situ SSA measurements have not been made. We anticipate from earlier papers [Husar *et al.*, 1997; Herman *et al.*, 1997] that dust and sea salt are the major aerosol components. The visible ($\approx 0.55 \mu\text{m}$) SSA for the sea salt is 1.0. For dust, however, the precise value of SSA is not known, and its value can vary significantly from one region to another. For example, the range extends from 0.65 to 0.70 [Tanre *et al.*, 1988; Sokolik and Toon, 1999], from 0.8 to 0.9

Table 1. Comparison of the Retrieved Aerosol Optical Depths With Tahnk's [2001] Results (at 0.63 μm) in $10^\circ \times 10^\circ$ Box With Kaashidhoo Climate Observatory (KCO) at Center^a

Year	KCO	Ours	Tahnk's
1996	...	0.16	0.19
1997	...	0.20	0.22
1998	0.13	0.13	0.17
1999	0.26	0.22	0.24
2000	0.17	0.19	0.21

^a A 3-month average for January, February, and March.

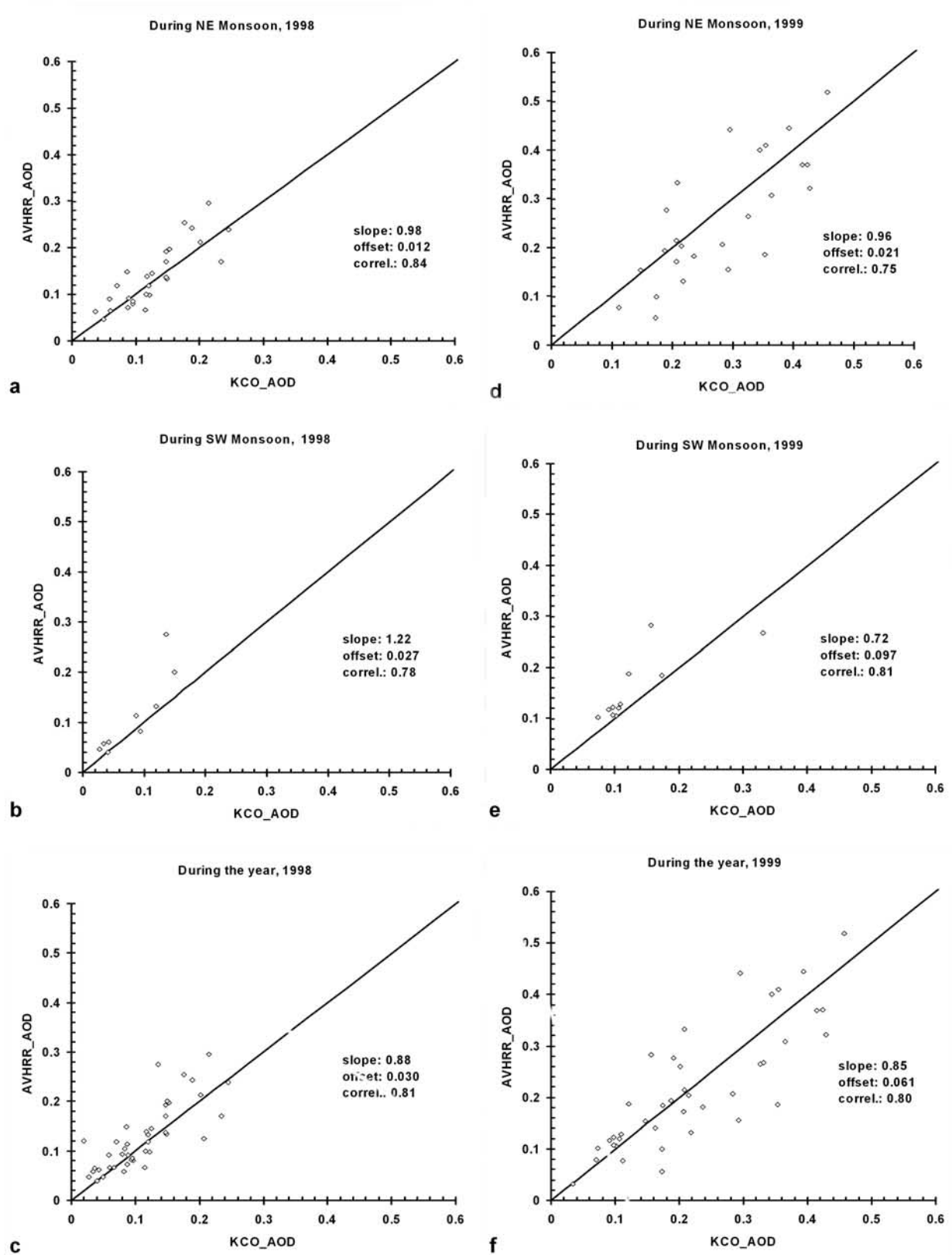
[Hess *et al.*, 1998], and from 0.9 to 1.0 [Fukushima and Toratani, 1997; Kaufman *et al.*, 2001]. In this paper, persuaded by the recent results of Kaufman *et al.* [2001], we adopt SSA of 0.95 at 0.55 μm . Furthermore, we assumed the SSA to be independent of RH.

[12] We wish to point out that the SSA adopted in this model is in excellent agreement with SSA retrieved by Dubovik *et al.* [2002] using Aerosol Robotic Network (AERONET) data. For Maldives, Dubovik *et al.* obtained SSA of 0.89 for wintertime, in good agreement with our value of 0.88. They have not retrieved summer value for Maldives. However, their value (0.94 \sim 0.96) at Bahrain and Solar Village (in Saudi Arabia) for desert dust and oceanic aerosols is in good agreement with the value (0.95) used in this paper.

[13] We adopt the following SSAs: 0.88 for winter-spring (approximately December–April) from INDOEX values: 0.92 for the transition months (May and November), and 0.95 for summer (approximately June–October). The phase function in the present study for winter is similar to the one used by Rajeev *et al.* [2000], except that for summer it is recalculated with dust, sea salt, and sulfates. We assume a mixture of 40% dust, 50% sea salt, and 10% sulfate. The assumed SSA of 0.95 applies to this mixture. The composite phase function for the mixture is not very sensitive to the assumed fractional concentration of these aerosol types. In addition, our phase function agrees to within 20% of the dust values given by Kaufman *et al.* [1994].

3. Validation

[14] Ground-based AOD measurements were made at the Kaashidhoo Climate Observatory (KCO) located on the island of Kaasihidhoo in the Maldives (see Satheesh *et al.* [1999] for a description of KCO). KCO was developed as part of INDOEX. Among the many instruments at KCO, is the automatic CIMEL Sun/sky radiometer. CIMEL is part of the AERONET [Holben *et al.*, 1998]. We collocate the AVHRR-AOD data with CIMEL AOD, within $\pm 1.0^\circ$ latitude and longitude and within a time interval of ± 60 min. We avoid the influence of land reflection from the 1-km-wide island by excluding satellite data within $\pm 0.15^\circ$ latitude and longitude. Figures 1a–1f compare the in situ AOD with AVHRR AOD. They are illustrated for the periods of the northeast (NE) monsoon (Figures 1a and 1d), the southwest (SW) monsoon (Figures 1b and 1e), and the whole year (Figures 1c and 1f) for 1998 and 1999. Overall, the retrieved AODs are in good agreement with the CIMEL values. The consistency between the two data is much better during the NE monsoon (winter) than during the SW



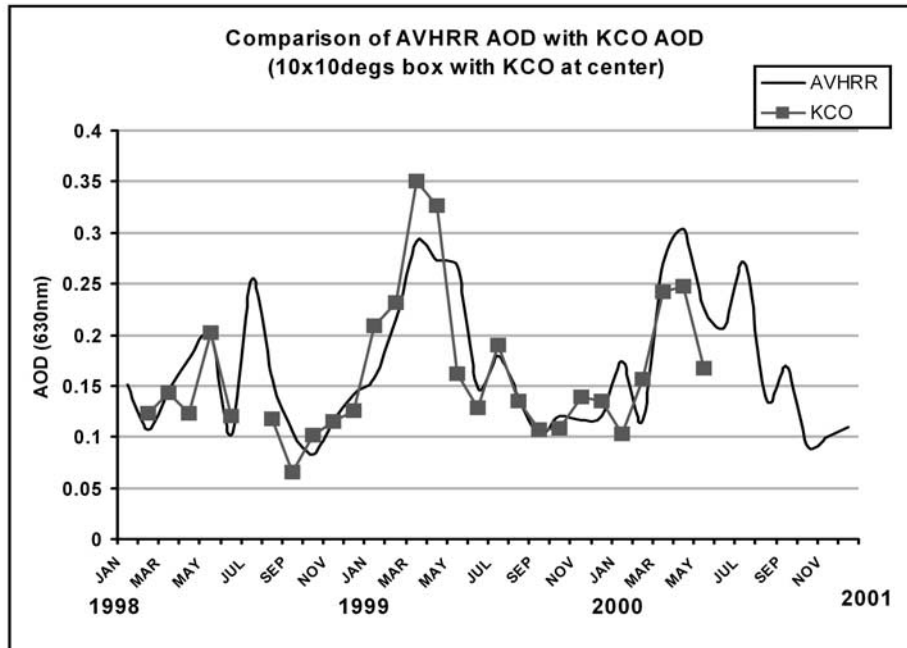


Figure 2. Comparison of the retrieved AOD with KCO measurements in $10^{\circ} \times 10^{\circ}$ box with KCO at center.

monsoon (summer). This should not be surprising since we used in situ chemical data for the NE monsoon as opposed to the best guess models for the other seasons. The slopes, the offsets, and the correlation coefficients (R) are listed in Figure 1. During the winter season the slopes between the CIMEL-AOD and the AVHRR-AOD are close to unity (0.97 on average), and the offsets are also smaller. For summer, however, the slopes vary between 0.72 and 1.22, and the offsets reach values as high 0.097. In situ experimental data for the aerosol size distribution and chemical composition are needed for further improvement of the retrieval.

[15] Error estimates show that for the winter monsoon the in situ measured SSA is 0.88 ± 0.02 for the column average [Ramanathan *et al.*, 2001]. The uncertainty in the retrieved AODs is $\pm 15\%$. Owing to lack of real measurements during the transition periods and the summer monsoon we can only provide best guesses for the uncertainty. The uncertainty of SSA is estimated to be about ± 0.03 . Uncertainty of the retrieved AODs is $\pm 20\%$ for the transition periods and $\pm 25\%$ for the summer monsoon. We also suggest that nonsphericity of the dust may be responsible for some of the differences between AVHRR-AOD and KCO-AOD during the SW monsoon.

[16] The AODs retrieved from the present scheme are considerably better than the standard operational AODs available through the National Oceanic and Atmospheric Administration (NOAA) web site (<http://www.saa.noaa.gov>).

The slope of the NOAA-AVHRR AOD versus the CIMEL AOD at KCO is usually < 0.6 , and the corresponding offset is > 0.08 . The success of our model is due to the use of observed SSA, the use of the phase function derived from in situ data, and the limitation of the analysis to the antisolar side [Rajeev *et al.*, 2000] of the satellite scan.

[17] Figure 2 compares the annual cycle of AODs for 1998, 1999, and 2000. The AVHRR AODs capture the annual cycle quite accurately. Table 1 compares the 3-month average of AODs for January, February, and March from 1996 to 2000, with Tahnk's [2001] AVHRR AODs. Tahnk's data are for a $10^{\circ} \times 10^{\circ}$ box with KCO at the center. Tahnk's scheme also accounts for the absorbing nature of the wintertime aerosol. The three data sets are in good agreement. In summary, the AODs retrieved in this study have the required accuracy (within $\pm 20\%$) to examine the role of the monsoonal circulation in the aerosol distribution.

4. Results and Discussions

4.1. Regional Distribution of AOD

[18] Spatial distributions of the monthly mean AODs are given in Figure 3 for 5-year averages (1996–2000). The AODs were derived for each pixel of 4×4 km resolution, which were then spatially and temporally averaged to a latitude and longitude bin of 1° resolution. Irrespective of the season, the AOD is significantly higher in the Northern Hemisphere compared to the Southern

Figure 1. (opposite) Comparison between the aerosol optical depth (AOD) at 630 nm measured at Kaashidhoo Climate Observatory (KCO) and retrieved from NOAA 14 advanced very high resolution radiometer (AVHRR) global area coverage data over the tropical Indian Ocean during the (a and d) northeast monsoon, (b and e) southwest monsoon, and (c and f) entire year in 1998 and 1999, respectively. Linear regression results of both the measured and the retrieved AODs are given in the slope, offset, and correlation coefficient.

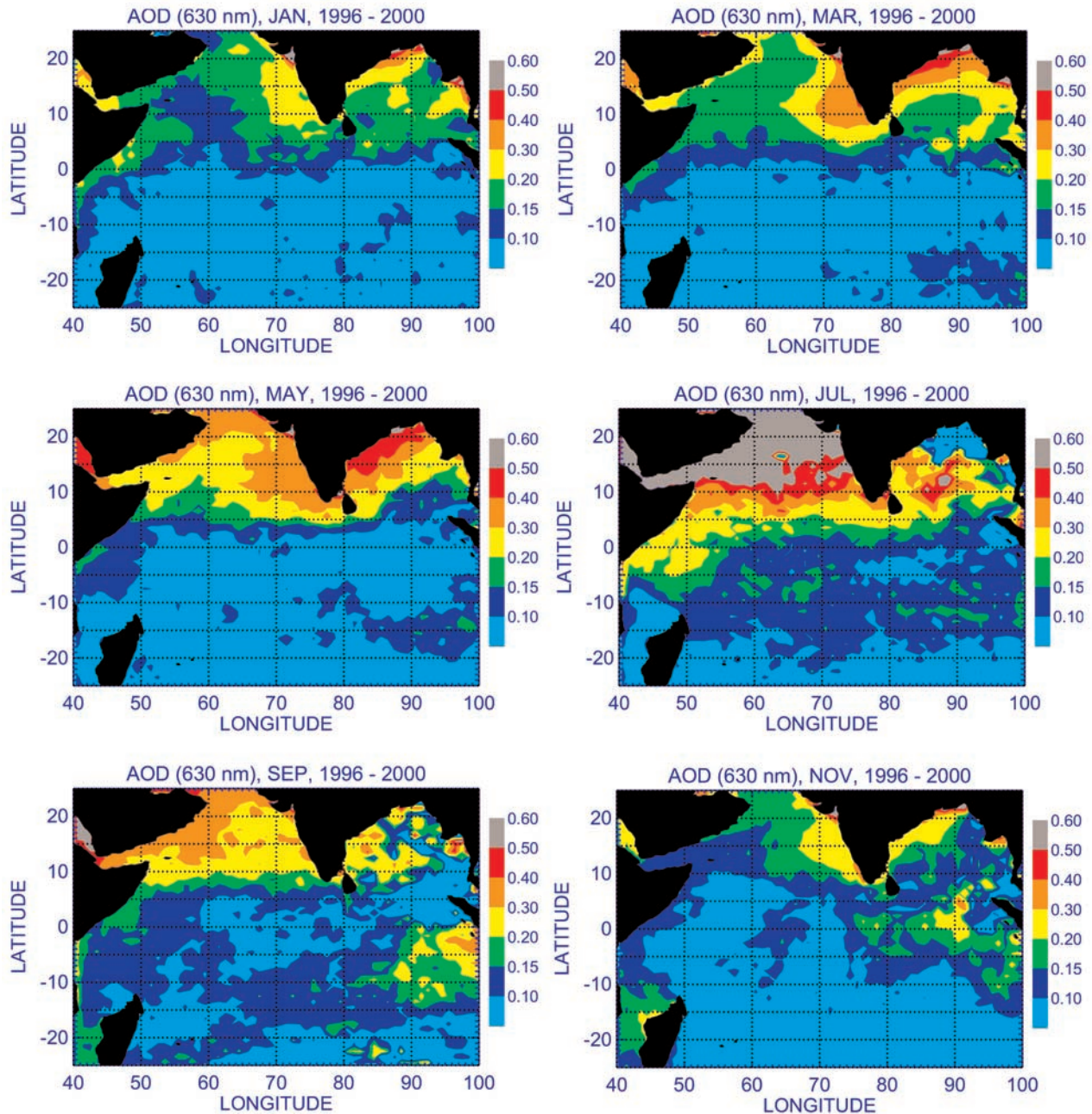


Figure 3. Maps of the monthly mean satellite-derived AOD over the tropical Indian Ocean in the period from January to November every other month, averaged for 5 years (1996–2000).

Hemisphere, with peak values of AOD near the coastal regions. Plumes of aerosol originating from the Arabian Peninsula, the Indian subcontinent, and Southeast Asia extend over most of the north Indian Ocean. In the Southern Hemisphere, AODs generally remain <0.1 , with one exception of a plume of high AODs near the coast of Sumatra in September.

[19] Figure 4 shows maps of AODs during the winter monsoon (January–March) and summer monsoons (June–August). Two major characteristics of the regional distribution can be identified from Figure 4. During the winter monsoon the AODs are larger over both the Arabian Sea

and the Bay of Bengal. As identified in numerous studies [e.g., *Rajeev et al.*, 2000; *Satheesh et al.*, 1999; *Ramanathan et al.*, 2001], the dominant sources for these aerosols are anthropogenic emissions (both biomass burning and fossil fuel combustion). Figure 5 shows the seasonal mean atmospheric circulation obtained from NCEP/NCAR reanalysis on surface for the winter and summer monsoon and at 700 hPa in 1999. The prevailing northeasterly near-surface winds (see Figure 5a) transport these aerosols over most of the north Indian Ocean. The second pattern is that seen during the summer monsoon, when AODs are much larger over the Arabian Sea compared with those over the Bay of

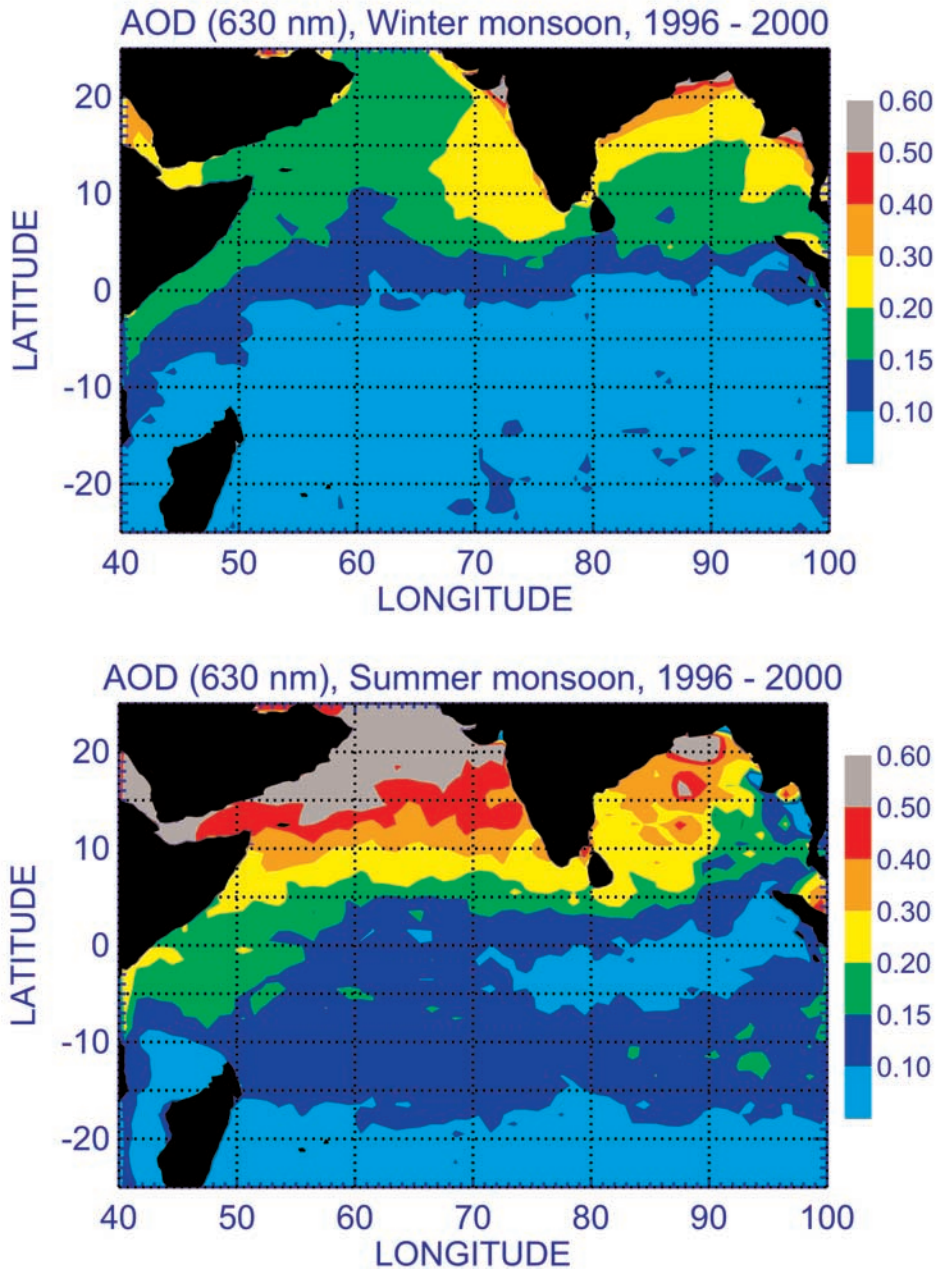


Figure 4. Maps of AODs during the (top) winter monsoon (January, February, and March) and (bottom) summer monsoon (June, July, and August), averaged for the 5 years from 1996 to 2000.

Bengal. With the onset of the southwest monsoon (see Figure 5b) the Arabian plume becomes dominant, and by June, AODs off the Arabian Peninsula and the north African coast reach values as high as 0.5–0.6 and spread to most of the Arabian Sea. Three factors contribute to the summer time aerosol buildup. First is the transport of mineral dust from Arabia and North Africa by the westerly winds at and above 700 mbar (see Figure 5c). Second is the enhancement in the production of sea salt by the strong westerly winds (Figure 5b). Last, the high humidity of the southwesterly surface winds (in the eastern Arabian Sea) increase the aerosol size, which, in turn, leads to an increase in scattering optical depth.

[20] During the transition months (April–May and September–November) the patterns are a hybrid mix of the two patterns described above. AOD distribution in the south Indian Ocean is also characterized by long-range transport of aerosol plumes originating from the surrounding landmasses. The continental influence is particularly strong during June–September, when AODs over the open ocean reach values as large as 0.2 between 10° and 20°S. The origin of these high values is most likely westward transport of biomass plumes from Indonesia and continental aerosols from Australia.

[21] Figure 6 shows an extreme case of heavy smoke plumes associated with episodes of the Indonesian brush

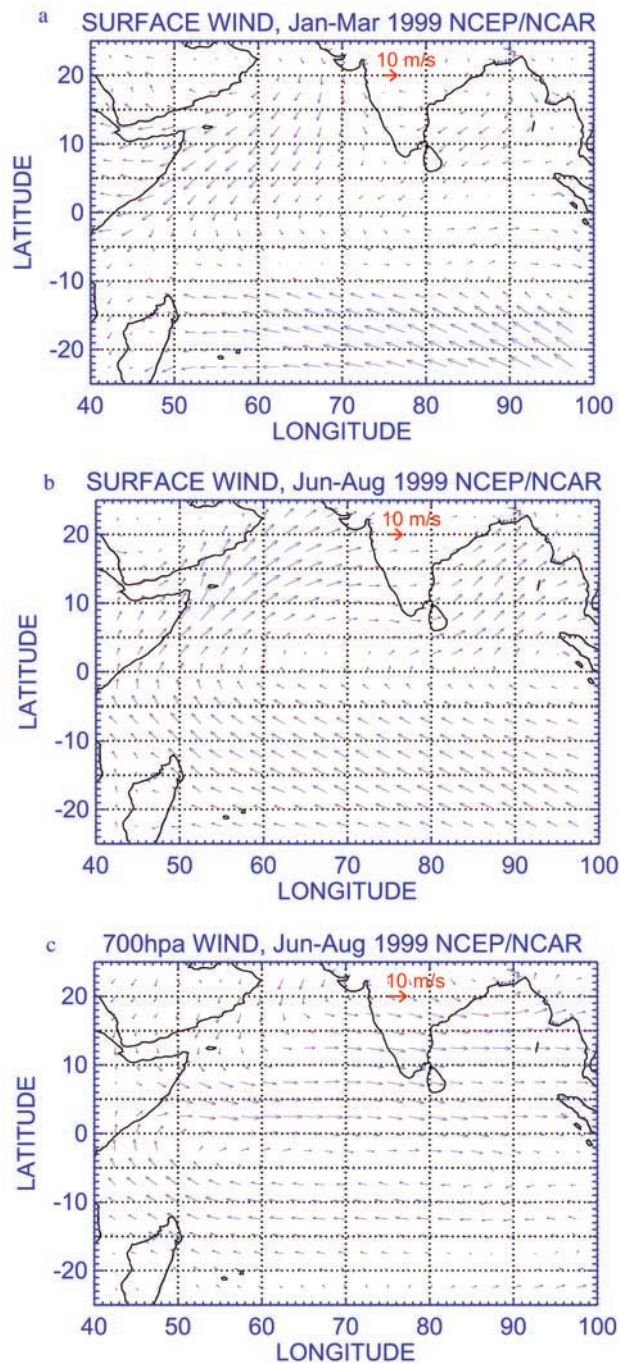


Figure 5. Prevailing seasonal mean atmospheric circulation (a) for the winter monsoon in January, February, and March and (b) for the summer monsoon in June, July, and August and (c) in the summer at 700 hPa based on the National Centers for Environmental Prediction/National Center for Atmospheric Research reanalysis from January through December 1999.

and forest fire in October 1997 (an El Niño year). During 1997 the seasonal rains were delayed by El Niño, which caused droughts in the western Pacific and major forest fires over Indonesia [Pearce, 1997, 1998]. The conflagration of 1997 was the most expensive bonfire in history, as the year's

El Niño was the most intense of the last century. The strong easterly or southeasterly wind flow transported the thick smoke aerosols over the equatorial zone and the south Indian Ocean. The fire lasted about 5 months, set in late July and doused briefly by monsoon rain in December [Pearce, 1998].

4.2. Annual Cycle

[22] The annual cycle is shown in Figure 7. The Arabian Sea has a distinct seasonal cycle (Figure 7a) with peak values in the summer months. The rest of the regions (Figures 7b–7d) have weaker amplitudes and different phases. The error bars display the maximum and minimum of monthly mean AODs and are an indication of interannual variability (discussed in more detail in section 4.3). The maximum monthly mean value (~ 0.6) of AOD during the summer is 3 times larger than that during the winter (0.2). The maximum AOD is comparable to the value (0.63) derived by Husar *et al.* [1997] for the 2-year data (1989–1991). A large fluctuation (0.2 \sim 0.4) occurs in May, because the transition of the monsoon from one type to another often occurs in this month.

[23] The Bay of Bengal cycle peaks in May (Figure 7b), whereas the south Indian Ocean AODs peak around September. For the Bay of Bengal (Figure 7b), AOD reaches maximum values in May, but the largest variations (as given by the error bars) are observed during June–August because of large interannual variations in rainfall. Aerosol seasonal variation over the equatorial belt is usually quite weak (seen in Figure 7c). The large interannual variability (also seen section 4.3) for October and November is associated with the episode of the 1997 Indonesian brush and forest fires [Jack and Eddy, 1999].

[24] Although the South Indian Ocean is far from the densely habited continents, it is still affected by the seasonal transport of injected aerosols. Figure 7d shows the seasonal variation of AOD over this area. It can be seen that AODs in the months of January through June are ~ 0.08 , a level of remote ocean background aerosols [Husar *et al.*, 1997]. During the period July to October the AODs rise to ~ 0.12 , associated with the westward transport of Indonesian smoke plumes. Several studies [Malingreau *et al.*, 1985; Husar *et al.*, 1997] showed that monthly averaged AODs in the Indonesia area have a strong pattern with peak values in September–October, which would help explain the September–October peaks in Figure 7d.

[25] The latitudinal profiles of AOD over the tropical Indian Ocean during the monsoon seasons are derived by averaging all the AOD values in the longitude range $40^\circ \sim 100^\circ\text{E}$. Figure 8 shows the latitudinal variation of AOD in the 5-year average from 1996 to 2000. The error bars display the standard deviation of the monsoon mean AODs.

[26] The general features revealed by Figure 8 are as follows: (1) The AOD in the Northern Hemisphere is larger than that in the Southern Hemisphere by a factor of ~ 5 . (2) The AOD maxima during both the NE monsoon and the SW monsoon are located at $\sim 20^\circ\text{N}$. (3) The northward migration of the AOD minima from winter monsoon to summer monsoon follows the migration of the ITCZ. (4) The AOD values in the latitude range $0^\circ \sim 18^\circ\text{S}$ during the SW monsoon are higher than that during the NE monsoon. The higher SW monsoon AOD in this range may be associated with the higher surface wind speed. The strong

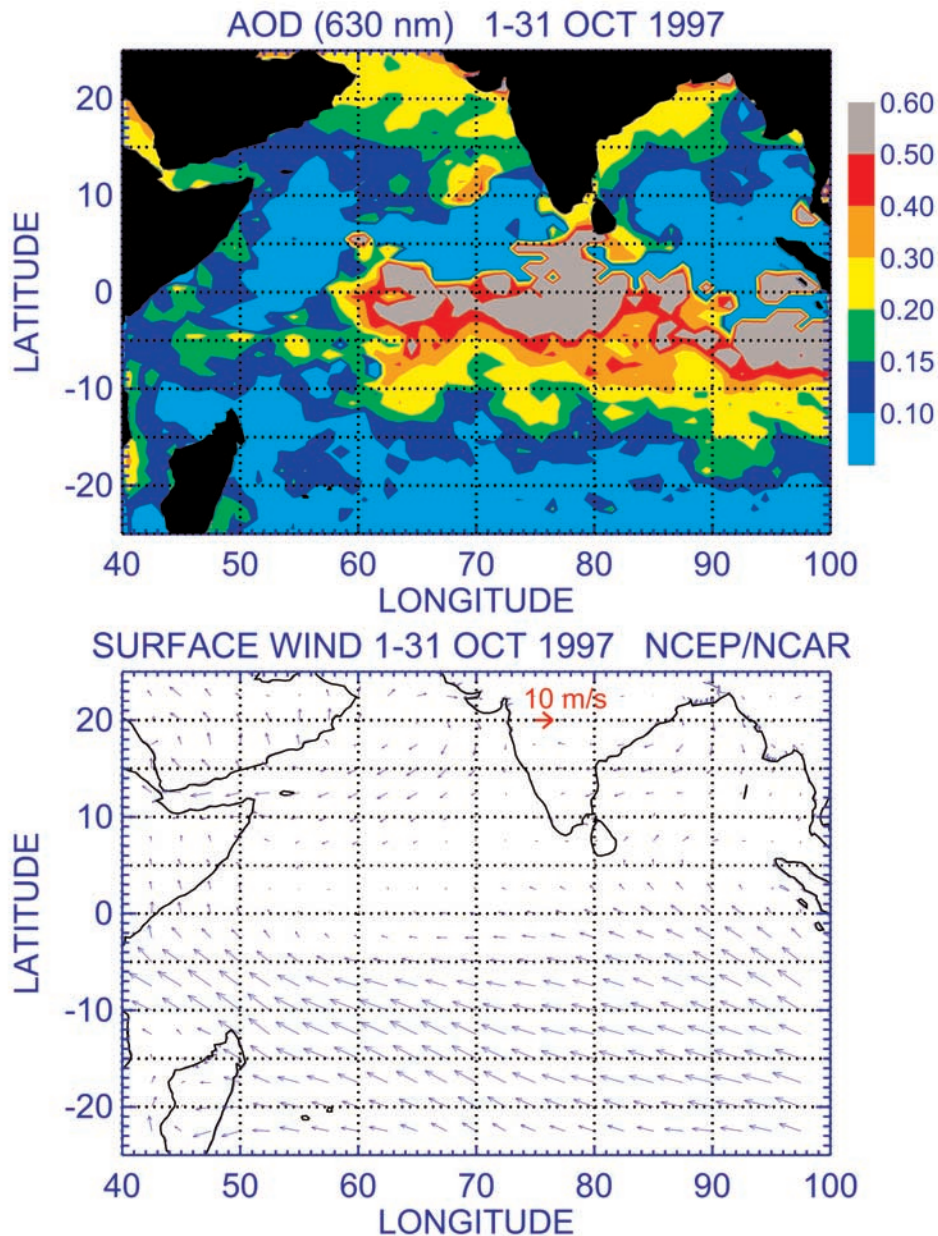


Figure 6. An extreme case for heavy smoke plumes over the equator with the Indonesian brush forest fire in October 1997.

wind (9 m/s averaged in this range, seen in Figure 5) in summer generates more sea salt aerosols than in winter (wind speed 4 m/s) [Krishna Moorthy *et al.*, 1997]. These patterns during the winter monsoon are confirmed by shipborne measurements, and a great hemispherical difference with high values of AOD in the 10° – 20° N region and a large latitudinal gradient in the aerosol concentration south of $\sim 10^{\circ}$ N were observed during the INDOEX cruise [Jayaraman *et al.*, 1998].

4.3. Interannual Variability

[27] The year-to-year variability of AODs during the SW monsoon and the NE monsoon is shown in Figure 9 along with the variability of the annual mean values. Interannual

variations of the SW monsoon AODs over the Bay of Bengal are largest, with a variability of $\pm 23\%$ of total annual AODs. The values for the other regions are $\pm 7\%$ over the Arabian Sea, $\pm 9\%$ over the equator belt, and $\pm 19\%$ over the South Indian Ocean, respectively. The variability during the NE monsoon is 7–16% and is $< 11\%$ for the yearly mean. Those phenomena may be related to the monsoon intensity. Analysis of monsoon intensity measured with the mean annual rain fall rate over India and its deviation from the long-term average (K. Raghavan, private communication, 2001) shows that the year 1997 was a strong monsoon year with anomaly rain fall of +2.19%, (+0.05% in 1996, -0.09% in 1998, -3.7% in 1999, and -8.0% in 2000, respectively). It is interesting that the

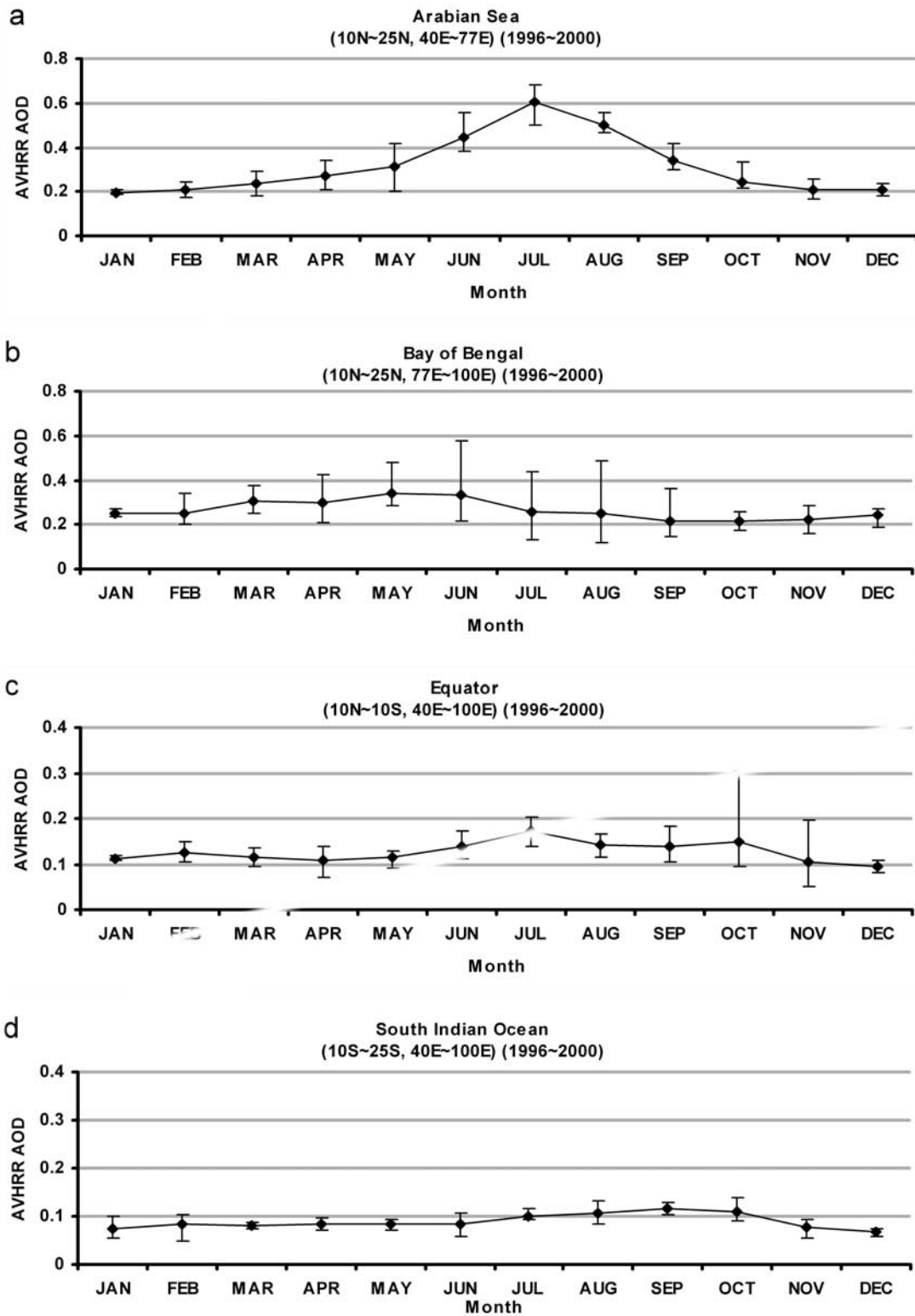


Figure 7. Monthly variation of the retrieved AOD averaged over the 5 years from 1996 to 2000 for the (a) Arabian Sea ($10^{\circ} \sim 25^{\circ}\text{N}$, $40^{\circ} \sim 77^{\circ}\text{E}$), (b) Bay of Bengal ($10^{\circ} \sim 25^{\circ}\text{N}$, $77^{\circ} \sim 100^{\circ}\text{E}$), (c) equator belt ($10^{\circ} \sim 10^{\circ}\text{S}$, $40^{\circ} \sim 100^{\circ}\text{E}$) (c), and (d) South Indian Ocean ($10^{\circ} \sim 25^{\circ}\text{S}$, $40^{\circ} \sim 100^{\circ}\text{E}$). The error bars indicate the range of the fluctuation of the monthly mean AOD each year.

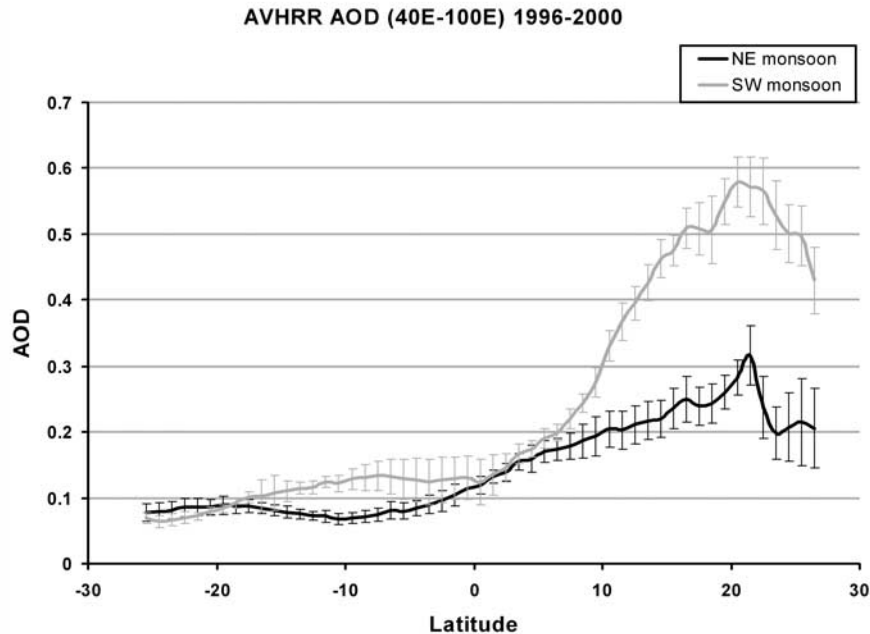


Figure 8. Latitudinal variations of the advanced very high resolution radiometer retrieved AOD during the winter (northeast) monsoon and the summer (southwest) monsoon averaged from 1996 to 2000.

AODs during 1997 were higher over both the Arabian Sea and the Bay of Bengal.

[28] The correlation of the AOD magnitude with the monsoon intensity is weak over the Arabian Sea (Figure 9a) because the AOD distribution over the Arabian Sea is more influenced by a dust transport from the Arabian Peninsula and the African region [Ackerman and Cox, 1989]. This has important implications for studies of the sedimentary record, as sedimentary composition of large parts of the Arabian Sea cannot be interpreted solely in terms of changes in SW monsoon intensity [Haake *et al.*, 1993].

[29] For the equator area (Figure 9c), interannual variations of the two monsoon AODs seem to be in harmony with those over the Arabian Sea, suggesting a major influence of the monsoon transport from the Arabian Sea. The variability of AODs over the south Indian Ocean (Figure 9d) is dominated by not only the monsoon interhemispheric transport [Krishnamurti *et al.*, 1998] but also by the Southern Hemisphere continental particle sources [Tegen and Miller, 1998]. A high SW monsoon AOD in 2000 over this area could be associated with the smoke plumes arising from Somalia and Indonesia [Ketterings and Bigham, 2000].

5. Conclusions

[30] Aerosol optical depths over the tropical Indian Ocean are derived from the NOAA 14/AVHRR data from 1996 to 2000. The retrieval is based on the aerosol model established at a central island of the region, i.e., Kasshidhoo Climate Observatory, one of the Aerosol Robotic Network (AERONET) stations. The seasonal modification of the aerosol SSA and the variability in sea surface reflectance due to daily variation in wind speed are taken into account in the aerosol retrieval. The regional distribution of AODs

and its comparison with the monsoonal flow reveal the following features:

1. During the winter monsoon, intense aerosol plumes are observed near the east and west coast areas of the Indian subcontinent. The northeastern winds bring continental aerosol offshore rushing over the Arabian Sea and the Bay of Bengal, forming a decrease gradient down to equator area. The low-level wind flow transports the boundary layer with a relatively small SSA. During the summer monsoon most of the transport takes place in deep atmospheric layers. Mid troposphere transport plays an important role in the AOD distribution over the Arabian Sea and the Bay of Bengal. Although the SW monsoon winds could carry dust from the Horn of Africa into the Arabian Sea, transport of aerosols from the Arabian Peninsula by atmospheric circulation is likely to be the major source of high concentration of aerosols over the Arabian Sea.

2. Aerosol distribution over the Arabian Sea displays a clear annual cycle with a maximum (0.60 ± 0.10) in summer months and a minimum (0.20 ± 0.05) in winter. AODs over the Bay of Bengal show a weak annual pattern, with a maximum (0.33 ± 0.10) and a minimum (0.22 ± 0.05) both occurring in the transition between winter and summer monsoon. An episode of heavy aerosol plume in October 1997 is observed over the equatorial belt, which is associated with the Indonesia El Niño-related fires.

3. Interannual variations of summer monsoon AODs are largest over the Bay of Bengal, with a variability of $\pm 23\%$ of total annual AODs. The summer monsoon AODs over the Bay of Bengal were higher during years of stronger monsoon. However, the monsoon AODs over the Arabian Sea do not always follow the trend of the monsoon strength, since the Arabian Sea is more influenced by dust transports from the Arabian Peninsula and the African continent.

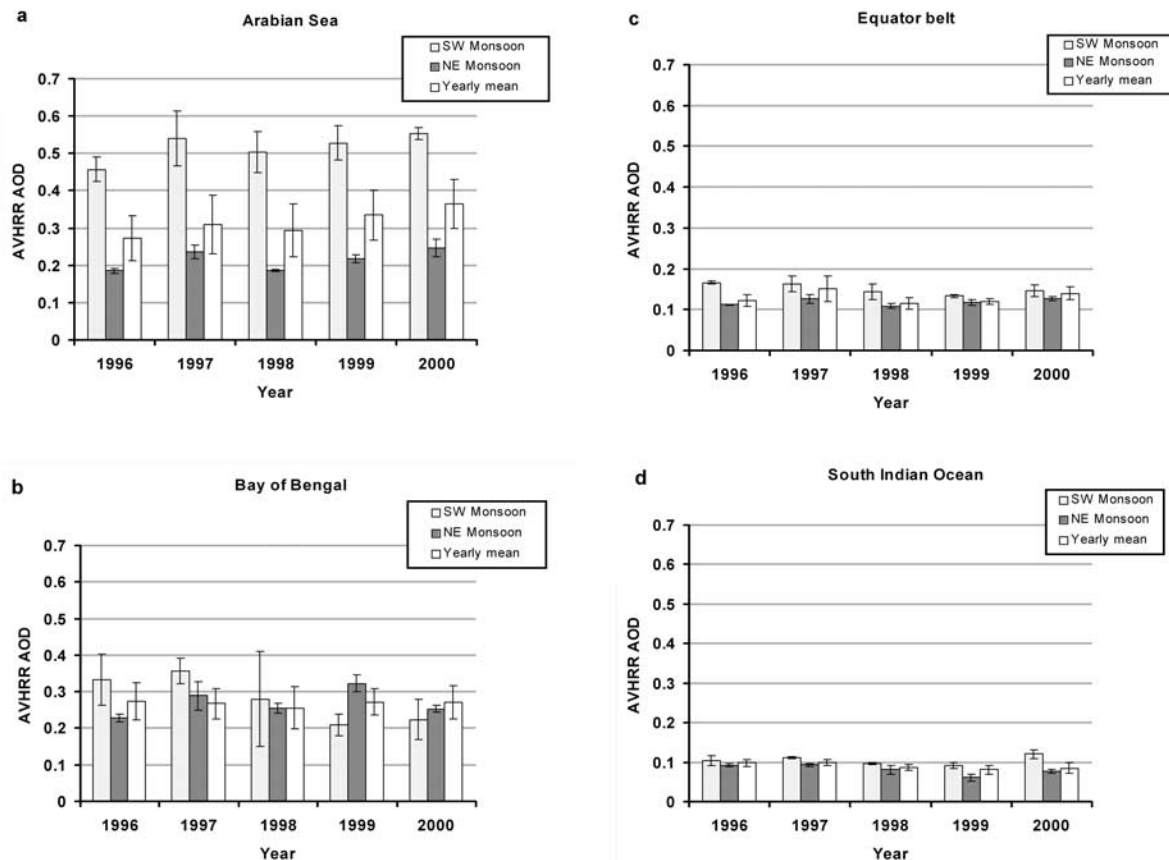


Figure 9. Interannual variations of AODs during the summer and winter monsoons and in yearly mean over the regions of the (a) Arabian Sea, (b) Bay of Bengal, (c) equator belt, and (d) south Indian Ocean. The error bars show the standard deviation of the retrieved AODs.

[31] Assessment of the role of aerosol in climate requires detailed knowledge of aerosol properties. This study provides spatial and temporal characteristics of aerosol optical depth derived from the AVHRR GAC data over the tropical Indian Ocean. We also show that the present AOD data are of better quality than the archived AVHRR AOD. However, the present retrieval algorithm is based on the aerosol model that was developed at one ground station, KCO, and in a limited duration. Multiple station observations, especially in situ measurements during the summer monsoon, will be needed to verify the satellite results.

[32] **Acknowledgments.** The wind vector data are provided by the NOAA Climate Diagnostics Center. The ground AOD measurements are from AERONET by B. Holben and his colleagues. The NCEP/NCAR reanalysis is provided by the NOAA Climate Diagnostic Center from their Web site at <http://www.cdc.noaa.gov>. The authors thank K. Rajeev for his help with the analysis and K. Raghavan for his monsoon rainfall data. This study was partially funded by the National Science Foundation (NSF) grant ATM 9612887.

References

Ackerman, S. A., and S. K. Cox, Surface weather observations of atmospheric dust over the southwest summer monsoon region, *Meteorol. Atmos. Phys.*, 41, 19–34, 1989.

- Che, N., and J. C. Price, Survey of radiometric calibration results and methods for visible and near infrared channels of NOAA-7, -9, and 11 AVHRRs, *Remote Sens. Environ.*, 41, 19–27, 1992.
- Cox, C., and W. Munk, Measurement of the roughness of the sea surface from photographs of the sunglitter, *J. Opt. Soc. Am.*, 44, 834–850, 1954.
- Dubovik, O., B. N. Holben, T. F. Eck, A. Smirnov, Y. J. Kaufman, M. D. King, D. Tanre, and I. Slutsker, Variability of absorption and optical properties of key aerosol types observed in worldwide locations, *J. Atmos. Sci.*, 59, 590–608, 2002.
- Duntley, S. Q., W. H. Wilson, and C. F. Edgerton, Detection of ocean chlorophyll from Earth orbit, in *Ocean Color Analysis*, edited by S. Q. Duntley et al., *SIO Ref. 74-10*, pp. 1–37, Scripps Inst. of Oceanogr., La Jolla, Calif., 1974.
- Fukushima, H., and M. Toratani, Asian dust aerosol: Optical effect on satellite ocean color signal and a scheme of its correction, *J. Geophys. Res.*, 102(D14), 17,119–17,130, 1997.
- Gordon, H. R., and D. K. Clark, Clear water radiances for atmospheric correction of coastal zone color scanner imagery, *Appl. Opt.*, 20(24), 4175–4180, 1981.
- Gordon, H. R., and M.-H. Wang, Retrieval of water-leaving radiance and aerosol optical thickness over the oceans with SeaWiFS: A preliminary algorithm, *Appl. Opt.*, 33(3), 443–452, 1994.
- Haake, B., V. Ittekkot, T. Rixen, V. Ramaswamy, R. R. Nair, and W. B. Curry, Seasonality and interannual variability of particle fluxes to the deep Arabian Sea, *Deep Sea Res., Part I*, 40(7), 1323–1344, 1993.
- Herman, J. R., P. K. Bhartia, O. Torres, C. Hu, C. Seftor, and E. Celarier, Global distribution of UV-absorbing aerosols from Nimbus 7/TOMS data, *J. Geophys. Res.*, 102(D14), 16,911–16,922, 1997.
- Hess, M., P. Koepke, and I. Schult, Optical Properties of aerosols and clouds: The software package OPAC, *Bull. Am. Meteorol. Soc.*, 79, 831–844, 1998.

- Holben, B. N., et al., AERONET: A federated instrument network and data archive for aerosol characterization, *Remote Sens. Environ.*, *66*, 1–16, 1998.
- Husar, R. B., J. M. Prospero, and L. L. Stowe, Characterization of tropospheric aerosols over the ocean with the NOAA advanced very high resolution radiometer optical thickness operational product, *J. Geophys. Res.*, *102*(D14), 16,889–16,909, 1997.
- Jack, J., and B. Eddy, The great El Niño of 1997–1998: Impact on precipitation and temperature, *Consequences Nature Implications Environ. Change*, *5*, 17–26, 1999.
- Jayaraman, A., D. Lubin, S. Ramchandran, V. Ramanathan, E. Woodbridge, W. D. Collins, and K. S. Zalpuri, Direct observations of aerosol radiative forcing over the tropical Indian Ocean during the January–February 1996 pre-INDOEX cruise, *J. Geophys. Res.*, *103*(D12), 13,827–13,836, 1998.
- Kaufman, Y. J., and B. N. Holben, Calibration of the AVHRR visible and near-IR bands by atmospheric scattering, ocean glint and desert reflection, *Int. J. Remote Sens.*, *14*, 21–52, 1993.
- Kaufman, Y. J., A. Gitelson, A. Karnieli, E. Ganor, R. S. Fraser, T. Nakajima, S. Mattoo, and B. N. Holben, Size distribution and scattering phase function of aerosol particles retrieved from sky brightness measurements, *J. Geophys. Res.*, *99*(D5), 10,341–10,356, 1994.
- Kaufman, Y. J., A. Smirnov, B. N. Holben, and O. Dubovik, Baseline maritime aerosol: Methodology to derive the optical thickness and scattering properties, *Geophys. Res. Lett.*, *28*(17), 3251–3256, 2001.
- Ketterings, Q. M., and J. M. Bigham, Soil color as an indicator of slash-and-burn fire severity and soil fertility in Sumatra, Indonesia, *Soil Sci. Soc. Am. J.*, *64*(4), 1826–1832, 2000.
- Kriebel, K. T., Cloud detection using AVHRR data, in *Advances in the Use of NOAA AVHRR Data for Land Application*, edited by G. D'Souza, A. S. Belward, and J. Malingreau, pp. 195–210, Kluwer Acad., Norwell, Mass., 1996.
- Krishna Moorthy, K., S. K. Satheesh, and B. V. Krishna Murthy, Investigation of marine aerosol over the tropical Indian Ocean, *J. Geophys. Res.*, *102*, 18,827–18,842, 1997.
- Krishnamurti, T. N., B. Jha, J. M. Prospero, A. Jayaraman, and V. Ramanathan, Aerosol and pollutant transport and their impact on radiative over the tropical Indian Ocean during the January–February 1996 pre-INDOEX cruise, *Tellus, Ser. B*, *50*, 521–542, 1998.
- Loeb, N. G., In-flight calibration of NOAA AVHRR visible and near-IR bands over Greenland and Antarctica, *Int. J. Remote Sens.*, *18*, 477–490, 1997.
- Malingreau, J. P., G. Stephens, and L. Fellows, Remote sensing of forest fires: Kalimantan and North Borneo in 1982–83, *Ambio*, *14*, 314–321, 1985.
- Moore, G. F., J. Aiken, and S. J. Lavender, The atmospheric correction of water color and the quantitative retrieval of suspended particulate matter in case II waters: Application to MERIS, *Int. J. Remote Sens.*, *20*, 1713–1733, 1999.
- Pearce, F., Incendiary policies (fires in Indonesia caused by land clearance), *New Sci.*, *156*(2102), 4–5, 1997.
- Pearce, F., Playing with fire (preventing forest fires in Indonesia), *New Sci.*, *157*(2126), 36–40, 1998.
- Rajeev, K., V. Ramanathan, and J. Meywerk, Regional aerosol distribution and its long-range transport over the Indian Ocean, *J. Geophys. Res.*, *105*(D2), 2029–2043, 2000.
- Ramanathan, V., et al., Indian Ocean Experiment (INDOEX), *White Pap. C4, Publ.143*, Scripps Inst. of Oceanogr., La Jolla, Calif., 1995.
- Ramanathan, V., et al., Indian Ocean Experiment (INDOEX), *White Pap. C4, Publ.162*, Scripps Inst. of Oceanogr., La Jolla, Calif., 1996.
- Ramanathan, V., et al., Indian Ocean Experiment: An integrated analysis of the climate forcing and effects of the great Indo-Asian haze, *J. Geophys. Res.*, *106*(D22), 28,371–28,398, 2001.
- Rao, C. R. N., and J. Chen, Inter-satellite calibration linkages for the visible and near-infrared channels of the advanced very high resolution radiometer on the NOAA-7, -9, and -11 spacecraft, *Int. J. Remote Sens.*, *16*, 21–52, 1995.
- Rao, C. R. N., and J. Chen, Revised post-launch calibration of the visible and near-infrared channels of the advanced very high resolution radiometer (AVHRR) on the NOAA-14 spacecraft, *Int. J. Remote Sens.*, *18*, 3485–3491, 1999.
- Satheesh, S. K., V. Ramanathan, X. Li-Jones, J. M. Lobert, I. A. Podgorny, J. M. Prospero, B. N. Holben, and N. G. Loeb, A model for the natural and anthropogenic aerosols over the tropical Indian Ocean derived from Indian Ocean Experiment data, *J. Geophys. Res.*, *104*(D22), 27,421–27,440, 1999.
- Saunders, R. W., and K. T. Kriebel, An improved method for detecting clear sky and cloudy radiances from AVHRR data, *Int. J. Remote Sens.*, *9*, 123–150, 1988.
- Sokolik, I. N., and O. B. Toon, Incorporation of mineralogical composition into models of the radiative properties of mineral aerosol from UV to IR wavelengths, *J. Geophys. Res.*, *104*(D8), 9423–9444, 1999.
- Tahnk, W. R., INDOEX aerosol optical depths and radiative forcing derived from AVHRR, Ph.D. thesis, Oreg. State Univ., Corvallis, 2001.
- Tanre, D., P. Y. Deschamps, C. Devaux, and M. Merman, Estimation of Saharan aerosol optical thickness from blurring effects in thematic mapper data, *J. Geophys. Res.*, *93*(D12), 15,955–15,964, 1988.
- Tegen, I., and R. Miller, A general circulation model study on the inter-annual variability of soil dust aerosol, *J. Geophys. Res.*, *103*(D20), 25,975–25,995, 1998.

F. Li and V. Ramanathan, Center for Atmospheric Sciences, Center for Clouds, Chemistry and Climate, Scripps Institution of Oceanography, University of California, San Diego, 9500 Gilman Drive, Mail Code 0221, La Jolla, CA 92093-0221, USA. (fli@fiji.ucsd.edu; ram@fiji.ucsd.edu)